Strong Sequestration of Hydrogen Into the Earth's Core During Planetary Differentiation

Liang Yuan[1] (ID) **and Gerd Steinle-Neumann[1]** (ID)

[1]Bayerisches Geoinstitut, Universität Bayreuth, Bayreuth, Germany

Abstract We explore the partitioning behavior of hydrogen between coexisting metal and silicate melts at conditions of the magma ocean and the current core–mantle boundary with the help of density functional theory molecular dynamics. We perform simulations with the two-phase and thermodynamic integration methods. We find that hydrogen is weakly siderophile at low pressure (20 GPa and 2,500 K), and becomes much more strongly so with pressure, suggesting that hydrogen is transported to the core in a significant amount during core segregation and is stable there. Based on our results, the core likely contains ~1 wt% H, assuming single-stage formation and equilibration at 40 GPa. Our two-phase simulations further suggest that silicon is entrained in the core-forming metal, while magnesium remains in the silicate phase. This preferred incorporation of silicon hints at an explanation for the elevated Mg/Si ratio of the bulk silicate Earth relative to chondritic compositions.

Plain Language Summary Hydrogen is the most abundant element in the universe and may be present in the Earth's core together with its main constituent, iron. Despite its importance, the amount of hydrogen in the core has been poorly understood as it is extremely difficult to measure the hydrogen content in iron metal from experiments at high pressure and temperature. Here, we use advanced quantum mechanical simulations on silicate and metallic melts showing that hydrogen becomes increasingly more incorporated in metal over silicate at high pressure and temperature, conditions under which Earth's core formed. Therefore, hydrogen can be present in the core in high abundance. We further show that silicon is also transported to the core to a smaller extent, while magnesium remains in the mantle material.

1. Introduction

The Earth's early accretion events, in particular magma ocean formation, had a great impact on the chemical and thermal evolution of the Earth. Segregation of metal from silicate to form a core during the magma ocean stage has removed elements besides iron and nickel from the mantle (e.g., Righter, 2003). Light elements such as H, C, O, and Si enter the core as a consequence of this process, which is supported by the observed density (ρ) deficit and sound velocity profiles in the core (e.g., Birch, 1952; Poirier, 1994; Wagle & Steinle-Neumann, 2019).

As the most abundant element in the universe, hydrogen is one of the candidates. Although its solubility in iron at atmospheric pressure (P) is very limited, the affinity of hydrogen to iron increases significantly under compression (Antonov et al., 1998; Badding et al., 1991; Fukai, 1984) as the Gibbs energy (G) of gaseous hydrogen increases rapidly with P. Solution of hydrogen in iron has been confirmed by neutron diffraction measurements (Ikuta et al., 2019; Machida et al., 2014) at high P, with H dissolving interstitially in Fe, expanding the lattice in a systematic way. The affinity to iron (siderophile behavior) at high P suggests that hydrogen is a strong candidate for the light element in the core. This is reflected by decades of work on the Fe–H system at high P, including melting point depression and phase diagram (Okuchi, 1998; Sakamaki et al., 2009), hydrogen partitioning experiments between silicate and iron (Clesi et al., 2018; Malavergne et al., 2019; Okuchi, 1997), and by extension studies of water–iron reactions (Fukai, 1984; Ohtani et al., 2005; Yagi & Hishinuma, 1995; Yuan et al., 2018). Recent diamond anvil cell (DAC) experiments reveal that a series of iron hydrides, e.g., FeH (Hirao et al., 2004; Isaev et al., 2007; Meier et al., 2019; Narygina et al., 2011), and compounds with higher H contents (Pépin et al., 2014, 2017) are thermodynamically stable at conditions relevant to the deep Earth.

Okuchi (1997) pioneered hydrogen partition experiments between molten iron and silicate at P to 7.5 GPa in the multi-anvil (MA) press to explore its distribution during core–mantle differentiation. Okuchi (1997)

suggested that > 95% of the H_2O present in a hydrous magma ocean may have reacted with Fe to form FeH_x, and ~60% of the ρ-deficit of the core can be accounted for by hydrogen as a light element. However, recent metal–silicate partitioning experiments by Clesi et al. (2018) and Malavergne et al. (2019) found hydrogen to be lithophile at high P and T, which shifted the debate of hydrogen in the Earth's core. Determining the hydrogen content of the metal in such experiments remains challenging as FeH_x decomposes during sample recovery from high P and T. Also, graphite was used as sample capsules, and recent DAC experiments (Hirose et al., 2019) suggest that C and H are mutually exclusive in molten iron. The presence of carbon may reduce the hydrogen storage capacity of iron, resulting in a very small equilibrium constant K_D between molten iron and silicate melt

$$K_D = \frac{\left(x_H^{met}\right)\left(1 - x_H^{sil}\right)}{\left(x_H^{sil}\right)\left(1 - x_H^{met}\right)}, \tag{1}$$

with x_H^{met} (x_H^{sil}) the mole concentrations of H in the metallic (silicate) melt.

Hydrogen metal–silicate partitioning data are only available at moderate P up to 21 GPa due to experimental challenges (Clesi et al., 2018; Malavergne et al., 2019; Okuchi, 1997). Here, we present results from molecular dynamics (MD) simulations using density functional theory (DFT) based methods on the interaction between hydrogen-bearing silicate and metallic liquids, determining hydrogen partitioning at 20–130 GPa and 2,500–4,000 K, which covers the whole range of P–T conditions of metal–silicate equilibration/segregation during core formation (Li & Agee, 1996; Siebert et al., 2012).

2. Computational Details

2.1. Density Functional Theory Molecular Dynamics Simulations

We conduct first-principles electronic structure calculations based on Kohn-Sham (KS) DFT to obtain total energy, Hellmann-Feynman stresses and forces with a plane wave approach and periodic boundary conditions using the Vienna *Ab Initio* Simulation Package (VASP) (Kresse & Furthmüller, 1996; Kresse & Hafner, 1993) with a planewave energy cutoff of 450 eV. We use the projector augmented wave implementation and atomic files (Kresse & Joubert, 1999) and the generalized gradient approximation to the exchange and correlation potential (Perdew et al., 1996). Electronic KS-DFT states are calculated at the Brillouin zone center only. Molecular dynamics (MD) simulations are performed in the canonical N–V–T ensemble, where the number of atoms (N) and the volume (V) of the cell are fixed, and T is controlled by a Nosé-Hoover thermostat (Hoover, 1985; Nosé, 1984). For the calculation of Helmholtz energy (F) using thermodynamic integration simulations (Section 2.3), the Nosé-Hoover thermostat is not stable when the system approaches the ideal gas limit with small distances between atoms, and we use the Langevin thermostat instead (Allen & Tildesley, 2017), following the approach of Dorner et al. (2018). After convergence of the electronic cycle, atoms are advanced with time steps of $\Delta t = 0.5$ fs due to the fast dynamics of hydrogen and – as for the thermostat – we change this to smaller $\Delta t = 0.2$ fs as we approach ideal gas behavior for TI. Initial structures of the liquids are generated by performing MD calculations at $T = 8,000$ K, which is then changed to the target T. We check that the cells considered are indeed in the molten state by monitoring the mean-square displacement (MSD) of all species and partial radial distribution functions (RDF) between them.

To obtain the volume of H_2O in metallic ($\overline{V}_M^H$) and silicate liquids ($\overline{V}_S^H$) at a given P and T, DFT-MD simulations are performed with supercells containing Fe_{50}, $(MgSiO_3)_{15}H_2O$, $Fe_{50}H_2O$ and $(MgSiO_3)_{15}$ in three P–T ranges: 5–25 GPa at 2500 K, 30–50 GPa and 120–140 GPa at 4000 K. The high-T P–V results are fitted by isothermal second-order Birch–Murnaghan equations-of-state (EoS) defined locally. $\overline{V}_M^H$ is obtained from the V-differences between Fe_{50} and $Fe_{50}H_2O$, and $\overline{V}_S^H$ between $(MgSiO_3)_{15}$ and $(MgSiO_3)_{15}H_2O$.

2.2. Two-Phase Simulation

Two-phase simulations model element partitioning directly, mimicking an experiment by putting metallic and silicate phases in direct contact in a simulation cell (SI, Figure S1), and then tracking the distribution of hydrogen atoms between the two liquids as the system approaches equilibrium. The two-phase technique has been widely used to study the melting T of different materials at high P (e.g., Alfè, 2005, 2009; Belonoshko & Dubrovinsky, 1996; Schwegler et al., 2008; Usui & Tsuchiya, 2010).

Initial configurations for our two-phase simulations are generated by independent DFT-MD simulations on single-phase hydrogen-bearing silicate liquid ($Mg_{37}Si_{37}O_{111}H_6$) and metallic iron melts with and without carbon ($Fe_{150}C_{30}H_6$ and $Fe_{150}H_6$,) at comparable P and identical T. Metal and silicate configurations are then combined into a single cell containing a total of 347 atoms ($Mg_{37}Si_{37}O_{111}H_6$–$Fe_{150}H_6$, MSH) and 377 atoms ($Mg_{37}Si_{37}O_{111}H_6$–$Fe_{150}C_{30}H_6$, MSHC) (SI, Figures S1a, S1b); a small gap between the metallic and silicate surfaces has to be introduced to avoid that distances between some atoms near the interface become too small. Even though hydrogen is likely present in its reduced oxidation state in silicate liquids under reducing conditions of deep magmas (Hirschmann et al., 2012), we also explore partitioning of hydrogen under oxidizing conditions by using the composition $Mg_{37}Si_{37}O_{114}H_6$–$Fe_{150}O_3H_6$ (MSHO) with 353 atoms (SI, Figure S1c). Configurations from the DFT-MD trajectory for each of the conditions considered (SI, Table S1) are analyzed in terms of the local atomic structure and spatial distribution of all atoms, in particular, their number density profile in the simulation box along the axis perpendicular to the phase boundary.

Although two-phase simulation are very straightforward, there are significant limitations to this method which highlight the need for additional calculations:

1. It is not appropriate for studying the partitioning behavior of atoms with similar or larger masses than those of the main elements constituting the silicate and metallic liquids (i.e., Mg, Si, O, and Fe). Hydrogen diffuses at least one order of magnitude faster than other kinds of atom in the melts (e.g., Posner & Steinle-Neumann, 2019).
2. To observe partitioning behavior, simulation T have to be moderate (here, 2,500–3,500 K), which ensures that hydrogen equilibrates between two coexisting phases, but prohibits extensive mixing of silicate and metallic phases. The mobility of heavy atoms can be enhanced substantially at high T, which leads to complete mixing of silicate (or silica) and metallic liquids, as observed in previous DFT-MD simulations in the Fe–Si–O ternary (Huang et al., 2019).
3. The two-phase simulation method can only provide qualitative results on metal–silicate partitioning of hydrogen (i.e., determine whether it is lithophile or siderophile) without the possibility to compute partitioning coefficients.

2.3. Thermodynamic Integration

We use the following reaction to evaluate hydrogen partitioning between the metallic liquid and silicate liquid:

$$(MgSiO_3)_{15}H_2O + Fe_{50} \leftrightarrow (MgSiO_3)_{15} + Fe_{50}H_2O, \tag{2}$$
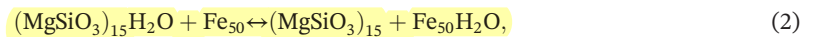
where we exchange H_2O rather than H_2 for computational convenience and as justified by the similar H behavior of the two-phase simulations for the MSH and MSHO systems (Section 3.1), and no inference is made concerning the nature of H speciation. The Gibbs energy change ($\Delta_r G$) of this reaction is

$$\Delta_r G = G\{(MgSiO_3)_{15}\} + G\{Fe_{50}H_2O\} - G\{(MgSiO_3)_{15}H_2O\} - G\{Fe_{50}\}. \tag{3}$$

The equilibrium constant of hydrogen defined in terms of the mole concentrations of H in the metallic and silicate melts (eq. 1) can then be calculated as

$$K_D = \exp \frac{-\Delta_r G}{k_B T}, \tag{4}$$

where k_B is the Boltzmann constant.

DFT-MD simulations give potential energy (U) and pressure (P) but not entropy (S) of the system; combining DFT-MD with the thermodynamic integration method provides a general scheme for computing the Helmholtz energy (F) difference $\Delta F = F_B - F_A$ of two systems containing the same number of atoms which are governed by different potential energy functions U_B (target system) and U_A (reference system) (e.g., Alfè et al., 2000; Vočadlo et al., 2008; Wahl & Militzer, 2015; Xiong et al., 2018). For the metal and silicate liquids considered in this study, we use the ideal gas as reference, for which F can be calculated analytically. We

perform a direct thermodynamic integration from ideal gas to the fully DFT interacting system at fixed V and T (Dorner et al., 2018; Rang & Kresse, 2019; Taniuchi & Tsuchiya, 2018):

$$F_B - F_A = \int_0^1 \left\langle \frac{\partial U\lambda}{\partial \lambda} \right\rangle_\lambda d\lambda, \tag{5}$$

where the notation $\langle A \rangle_\lambda$ signifies the thermodynamic average of quantity A over an ensemble generated by the Hamiltonian $H(\lambda)$ for which the potential energy $U(\lambda)$ term is a linear mixture of U_A and U_B ($U(\lambda) = (1 - \lambda)\,U_A + \lambda\,U_B$), with λ a coupling constant that connects the reference to the target system. The advantage of this method is that it expresses ΔF in terms of an ensemble average, which – unlike F or G – can be calculated directly in a simulation (Frenkel & Smit, 2001):

i. A system with potential energy function $U(\lambda)$ is simulated at a series of λ values. The derivative of U with respect to λ is then averaged over thermodynamically equilibrated configurations.
ii. Separate standard DFT-MD simulations are performed to locally determine isothermal EoS of the system (Section 2.1; SI, Figure S2).
iii. Numerical integration with respect to λ is carried out to obtain ΔF between the ideal gas and KS-DFT system.
iv. Once ΔF and absolute F are computed by adding the ideal gas contribution F_{ig}, G can be calculated by adding a PV term, i.e., $G = F + PV$. The EoS obtained in step (ii) are used to calibrate all the calculations to constant P, following the fundamental thermodynamic relation for G along an isotherm:

$$G(P_2, T) - G(P_1, T) = \left(\int_{P_1}^{P_2} V dP \right)_T. \tag{6}$$

DFT-MD simulations with various λ parameters for each of the compositions indicated in reaction 2 are performed at 20 GPa (2,500 K), and 40 GPa and 130 GPa (4,000 K) (SI, Figure S3) as indicated in Tables S2–S5 in the SI.

3. Results and Discussion

3.1. Two-Phase Simulations

Representative snapshots of the two-phase simulation results for the MSH, MSHC and MSHO compositions at two P–T conditions are shown in Figure 1 (SI, Table S1), animations for the development of the cells at all P–T conditions can be found in the supporting online material (SI, Movie S1). Simulations start from initial configurations where six hydrogen atoms each are located in the silicate (H_S) and metallic (H_M) liquids. At all P–T conditions considered, we observe the diffusion of hydrogen atoms from the silicate to the metallic phase, leading to an accumulation of hydrogen in iron (SI, Figure S4 and Movies S2–S4) that is also documented by the time-development of the partial radial distribution function (RDF) $g(r)$ between both hydrogen species (H_S and H_M) and Fe and O, i.e., $g_{OH_S}(r)$, $g_{OH_M}(r)$, $g_{FeH_S}(r)$ and $g_{FeH_M}(r)$ (SI, Figure S5).

At 21 GPa and 2,500 K, the number of hydrogen atoms in the metallic phase becomes larger than that in the silicate within 5 ps, but a few hydrogen atoms remain in the silicate over the entire simulation period of ~20 ps (Figures 1; SI, Figure S4 and Movies S1–S4). This is also reflected in the development of the RDF (SI, Figure S5 for the MSH system), where the amplitude of the principal peak in $g_{OH_S}(r)$ decreases rapidly with time and the principal peak in $g_{FeH_S}(r)$ emerges concurrently as a result of H atoms moving from the silicate to iron. By contrast, the interaction between H_M and Fe, and between H_M and O does not change with time as H_M atoms remain in the metallic phase. Nevertheless, the principal peak in $g_{OH_S}(r)$ remains noticeable even after 20 ps at 21 GPa and 2,500 K, suggesting a weakly siderophile character of hydrogen. At the three other P–T conditions explored (40 GPa, 2,800 K; 75 GP, 3200 K and 140 GPa, 3,500 K; SI, Table S1), all hydrogen atoms in the silicate phase move into the metallic phase within 10 ps and stay there.

By also monitoring the distribution of hydrogen in the systems containing carbon (MSHC) and oxygen (MSHO) in the metallic liquid (Figures 1; SI, Movie S1), the two-phase results show that the siderophile nature of hydrogen established for MSH does not change. The initially small interaction between O and H_M identified in the $g_{OH_M}(r)$ disappears completely; similarly, the principal peak in $g_{OH_S}(r)$ vanishes with time.
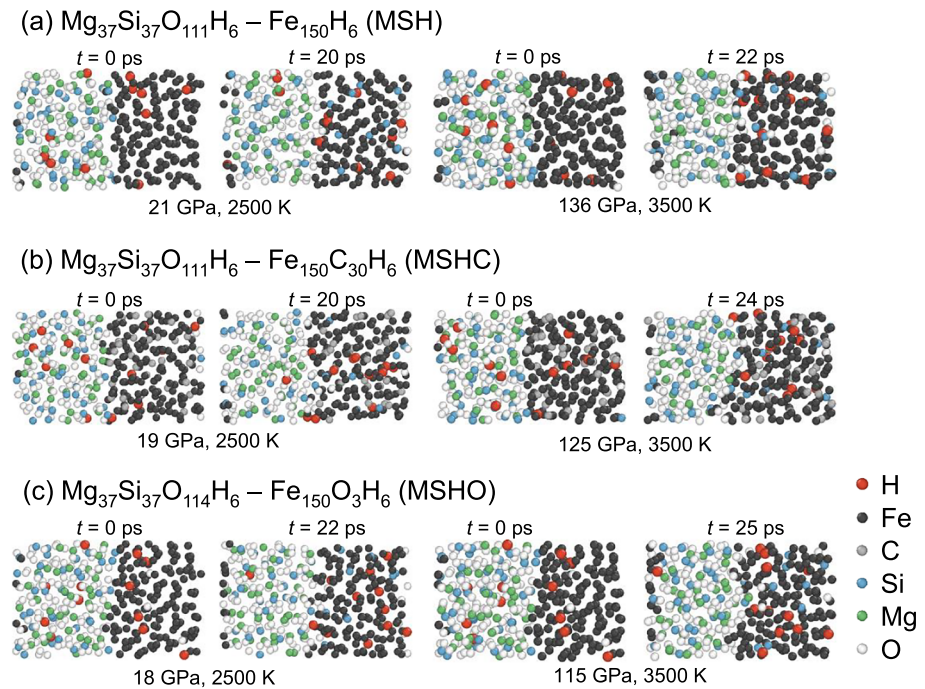
Figure 1. Initial and final configurations for the two-phase simulations of silicate and metal liquid in contact. The initial configurations for our simulations were generated by performing independent DFT-MD simulations on single-phase H-bearing silicate and metal liquids at comparable P and identical T (SI, Figure S1). Metal and silicate configurations were then combined into a single cell containing a total of (a) 347 atoms for $Mg_{37}Si_{37}O_{111}H_6$–$Fe_{150}H_6$ (MSH system), (b) 377 atoms for the carbon-bearing system $Mg_{37}Si_{37}O_{111}H_6$–$Fe_{150}C_{30}H_6$ (MSHC system) and (c) 353 atoms for the oxygen-bearing $Mg_{37}Si_{37}O_{114}H_6$–$Fe_{150}O_3H_6$ (MSHO system). The simulation duration is 20–25 ps (SI, Table S1). Animations for the development of the cells at all P–T conditions can be found in the supporting online material (SI, Movie S1).

3.2. H$_2$O Volume in Silicate and Metallic Melts

The molar volume of water in the metal $\overline{V}_M^H$ is predicted smaller than that in the silicate $\overline{V}_S^H$ in the DFT-MD simulations at all three P–T conditions considered further in thermodynamic integration (Figures 2a–2c) which constitutes an important aspect in the stronger affinity of hydrogen to metallic liquids relative to silicate melts. The volume difference $\Delta_r V$ for reaction 2

$$\Delta_r V = \overline{V}_M^H - \overline{V}_S^H, \tag{7}$$

decreases significantly at low P (5–25 GPa range) for the 2,500 K DFT-MD simulations, from −36% 5 GPa to −8% at 20 GPa for $\Delta_r V/\overline{V}_S^H$. This is due to the fact that the silicate melt structure undergoes radical atomic arrangement from four- to six-fold Si-O coordination (SI, Figure S6a): While the nearest neighbor O-H distance represented by the principal peak position in $g_{HO}(r)$ (SI, Figure S6b) remains at virtually the same distance, the second neighbor O-H distances are shifted to considerably lower r with increasing P, reflected in the decrease of $\overline{V}_S^H$ with P. By contrast, the average interatomic distance between Fe and H in the metallic melts remains constant over the same P-range (SI, Figure S6d), similar to the results reported in a previous DFT-MD study (Posner & Steinle-Neumann, 2019). At higher P, differences are $\Delta_r V/\overline{V}_S^H = -16\%$ (40 GPa, 4,000 K) and −12% (130 GPa, 4,000 K), and they contribute more significantly to G by a $P\Delta_r V$ energy component due to large P: The $P\Delta_r V$ term increases from −0.13 eV at 20 GPa and 2,500 K, to −0.54 eV at 40 GPa and 4,000 K, and −0.88 eV at 130 GPa and 4,000 K (Figures 2d–2f; SI, Table S2).

3.3. Thermodynamic Integration

Thermodynamic parameters corresponding to different hydrogen partitioning conditions are summarized in Tables S2–S5 in the SI. Figure S7 in the SI shows the variation of the radial distribution function $g_{SiO}(r)$ for
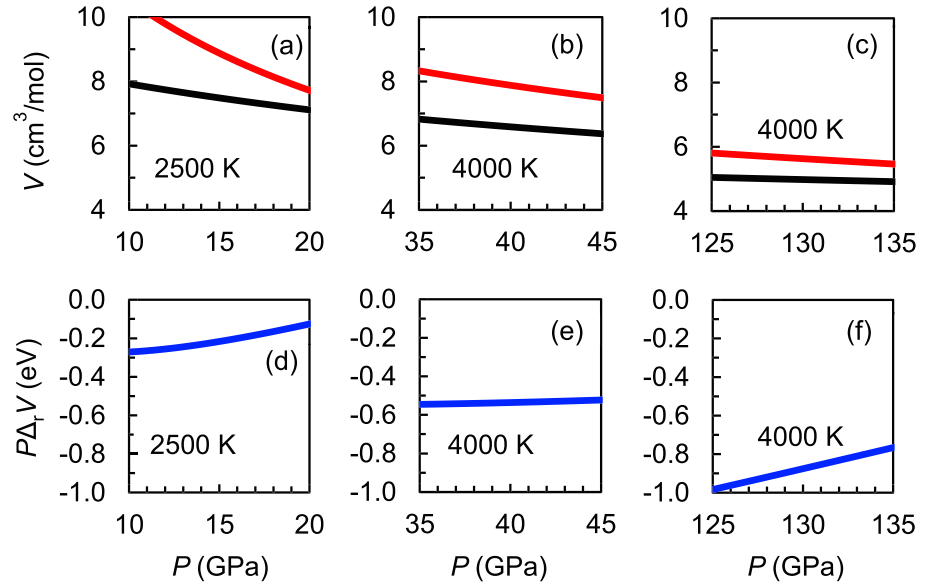
Figure 2. (a–c) Partial molar volume for H_2O in the silicate (red lines) and iron liquids, determined by a comparison of the results for $(MgSiO_3)_{15}H_2O$ vs. $(MgSiO_3)_{15}$ and $Fe_{50}H_2O$ vs. Fe_{50} at the three P–T conditions considered in the thermodynamic determination of the equilibrium constant for H_2O in silicate vs. metallic melts from DFT-MD simulations (SI, Table S2). (d–f) $P \cdot \Delta_r V$ contribution to the Gibbs energy change in reaction 2.

the $(MgSiO_3)_{15}H_2O$ liquid and $g_{FeFe}(r)$ for the $Fe_{50}H_2O$ liquid with changes in λ at 20 GPa and 2,500 K. As λ decreases, the first peak in $g(r)$ decreases in amplitude, becomes broader, and tends to shift to a smaller distance, to finally disappears at $\lambda < 0.0097$, reflecting ideal gas behavior.

Potential energy differences between the ideal gas and DFT liquid as a function of λ are shown in Figure S8 in the SI, with a smoothly varying integrand of eq. 5 at $\lambda \geq 0.0097$, and a strong increase for smaller λ. In order to perform the integration, a variable transformation $\lambda(x) = \left(x + \frac{1}{2}\right)^{1/(1-k)}$ ($\lambda \in [0,1] \to x \in [-1,1]$) is done (Dorner et al., 2018), and eq. 5 becomes

$$\int_{-1}^{1} f[\lambda(x)]\frac{d\lambda(x)}{dx}dx = \frac{1}{2(1-k)}\int_{-1}^{1} f[\lambda(x)]\lambda(x)^k dx. \quad (8)$$

This transformation is chosen such that the transformed functional $f[\lambda(x)]\lambda(x)^k$ can be set to 0 at $x = -1$. Using Gauss-Lobatto quadrature, the integral becomes a sum

$$\frac{1}{2(1-k)}\int_{-1}^{1} f[\lambda(x)]\lambda(x)^k dx = \frac{1}{2(1-k)}\sum_{i=1}^{n} \omega_{x_i} f[\lambda(x_i)]\lambda(x_i)^k, \quad (9)$$

where we chose $k = 0.8$ and a node number of $n = 8$, again following Dorner et al. (2018).

Calculated $\Delta_r G$ and hydrogen metal–silicate equilibrium constant (expressed as $\log_{10}K_D$, eq. 4) are shown in Figure 3 and given in Table S6 in the SI. The predicted K_D value at 20 GPa (2,500 K) agrees with partition experiments of Okuchi (1997) at 7.5 GPa, and is in reasonable agreement with the experiments of Clesi et al. (2018) at $P \sim 20$ GPa (SI, Table S6), although our results suggest a slightly stronger siderophile behavior. Differences in partitioning of hydrogen between the experiments by Okuchi (1997), on the one hand, and Clesi et al. (2018) and Malavergne et al. (2019), on the other hand, stem from the fact that Okuchi (1997) accounts for bubble volume in the recovered metal that
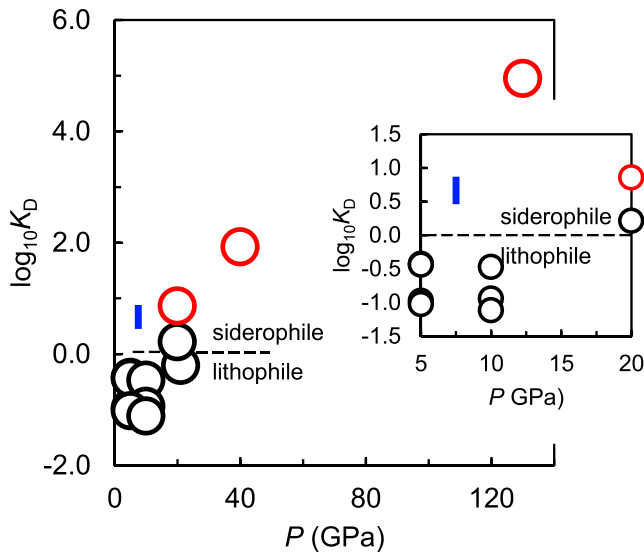

Figure 3. Hydrogen equilibrium constant computed from Gibbs energy differences from the DFT-MD simulations (eq. 4) for 20 GPa and 2,500 K, 40 GPa and 4,000 K and 130 GPa and 4,000 K (red circles) (SI, Table S6). Experimental data by Clesi et al. (2018) (black circles) and Okuchi (1997) (blue bar) are shown for comparison.

reflects exsolved hydrogen during quench due to its low solubility in solid Fe at ambient conditions (Antonov et al., 1998, 2019; Fukai & Suzuki, 1986). Hirose et al. (2019) and Umemoto and Hirose (2020) similarly arrive at the conclusion that the experiments by Clesi et al. (2018) and Malavergne et al. (2019) underestimate the hydrogen content in the metal.

As we increase P to 40 GPa and T to 4,000 K, our results predict that the vast majority of hydrogen partitions into the metallic melt, leaving only 2% hydrogen in the coexisting silicate melt. Zhang and Yin (2012), by contrast, predicted hydrogen to be slightly lithophile at comparable P–T conditions. This discrepancy is likely due to the large interface-to-volume ratio of the two-phase model in Zhang and Yin (2012), which could induce major artifacts (Hong & Van De Walle, 2013). At 130 GPa and 4,000 K, K_D is predicted to be exceedingly large such that the amount of hydrogen in silicate melt is negligible.

One should bear in mind that $\Delta_r G$ of exchanging an H_2O composition between silicate and metallic melts in reaction 2 as listed in Table S6 of the SI is very small compared to those typically associated with chemical reactions: for the reaction $(CO)_{50} + (O_2)_{25} \rightarrow (CO_2)_{50}$ in the gaseous phase, for example, $\Delta_r G = 130$ eV (at 298 K, 1 bar) (Atkins et al., 2010). This raises the question of uncertainties in calculating $\Delta_r G$ (and consequently K_D). The biggest source of uncertainty is the statistical fluctuation of U in DFT-MD simulations (for all λ in the thermodynamic integration). An uncertainty of 5 eV (~2%) in G for each of the components in reaction 2 translates to 10 eV for $\Delta_r G$, with severe consequences for values of K_D: at 20 GPa and 2,500 K, $\log_{10} K_D$ would vary between −19 and 21. In order to decrease the error, two approaches would be useful:

i. Larger simulation cells, with the goal to increase the number of exchanged H_2O, would decrease statistical fluctuations (increased precision).
ii. Simulations for F on a larger set of V–T points, with the goal to achieve higher accuracy by fitting physically motivated EoS models on this set, following prior work on silicate (de Koker & Stixrude, 2009) and metal liquids (Vlček et al., 2012).

However, both of these approaches require computational resources that are beyond current capabilities. Nevertheless, an empirical evaluation of our results by computing $\Delta_r G$ of reaction 2 over shorter run durations of the DFT-MD trajectory shows negligible changes that do not influence $\log_{10} K_D$ values.

4. Implications for Core Composition

4.1. A Hydrogen-Rich Earth's Core

Using two independent computational approaches within the general framework of DFT-MD, two-phase simulations and thermodynamic integration, we predict that hydrogen strongly partitions into liquid metal over silicate, with P leading to a strong increase in the equilibrium constant (Figure 3). In a planetary context, this implies that for a geochemically reasonable hydrogen content of the primitive mantle (~1,000 ppm H_2O) (e.g., Palme & O'Neill, 2013; Rubie et al., 2015) and assuming metal–silicate equilibration at $P \sim 40$ GPa (Li & Agee, 1996; Siebert et al., 2012) for single-stage core formation, the hydrogen content in the core is close to 1 wt% H. This amount of hydrogen, together with some amounts of other light elements (e.g., Si, *cf.* Section 4.2), is consistent with the requirement to match ρ and velocity of the Earth's core (Umemoto & Hirose, 2020). It is further helpful to maintain the outer core in the molten state at relatively low T (Nomura et al., 2014; Sakamaki et al., 2009). However, it remains contentious whether Earth accreted wet or dry. In the latter case, as favored by the late veneer hypothesis (e.g., Albarède, 2009; Righter, 2003; Wang & Becker, 2013), no significant amount of water was incorporated into the core during differentiation.

Hydrous minerals such as δ-AlOOH, phase-H $MgSiO_2(OH)_2$, and their solid solutions have been shown to be stable over the entire range of lower-mantle P–T conditions (Duan et al., 2018; Ohira et al., 2014; Sano et al., 2008; Walter et al., 2015), and could therefore transport water into the lowermost mantle in a subducting slab. With the steep T-increase in the D" layer just above the CMB, these hydrous phases are likely to undergo dehydration, leading to hydrous silicate melts. Previous DFT-MD simulations (Bajgain et al., 2015; Mookherjee et al., 2008) suggest that such hydrous silicate melts are neutrally or negatively buoyant and therefore gravitationally stable at the base of the lower mantle, inhibiting efficient upward transport of volatiles through the mantle. In such a scenario, given the large value of K_D at CMB conditions (Figure 3), the core would serve as an infinite sink for any hydrogen that comes in contact with it.

4.2. Mg/Si Fractionation Due to Core Formation

Beyond the preferred partitioning of H into the metallic melt, our two-phase simulations reveal a substantially different distribution of Si and Mg (SI, Figure S9) with a significant number of Si atoms (e.g., 8–10/37 for 41 GPa and 2,800 K in the MSH system) stably present in the metal for the last ~5 ps of the atomic trajectories, while all Mg atoms remain in the silicate portion of the simulation cell. The absence of Mg from the metallic melts is not surprising, as our simulations were conducted at relatively low T that prohibit extensive mixing of silicate and metallic phases (Arveson et al., 2019; Huang et al., 2019). As Mg and Si have comparable diffusion coefficients (SI, Figure S10 and Table S7), the difference in behavior cannot be associated with their dynamics. Rather, their varying solution in Fe has to be associated with the fact that Mg has a weaker chemical affinity to metallic liquids than Si. Chemical reactions between metal and silicate investigated by DAC experiments (Badro et al., 2016; Takafuji et al., 2005) have shown that Mg solubility in liquid iron is extremely low for equilibration below 3,000 K, while up to 3 wt% Si dissolve into liquid iron, supporting the inference of our simulations.

This suggests sequestration of Si over Mg from the magma ocean during core formation, which in turn could explain the difference in the Mg/Si ratio between the chondritic value of ~1.0 (Allègre et al., 1995) and that of the bulk silicate Earth (~1.25) (McDonough & Sun, 1995), supporting the hypothesis of Si incorporation in the core (e.g., Georg et al., 2007; Shahar et al., 2009) over Si enrichment in the lower mantle (e.g., Murakami et al., 2012).

5. Conclusions

We present results from two-phase and thermodynamic integration simulations based on density functional theory molecular dynamics that model hydrogen partitioning between liquid silicate and metal. The two-phase simulations show strong accumulation of hydrogen in the metallic portion of the simulation cell that we quantify in terms of an equilibrium constant K_D by thermodynamic integration. Despite significant uncertainty, we find strong evidence for a moderately siderophile behavior of hydrogen at low pressure (20 GPa and 2,500 K), in quantitative agreement with the experiments by Okuchi (1997) and in qualitative agreement with the experiments of Clesi et al. (2018) at ~20 GPa. We further describe a strong increase in K_D with pressure, suggesting that hydrogen is strongly enriched in the core-forming metal during magma ocean segregation.

The two-phase simulations indicate non-negligible transfer of Si from the silicate to the metallic liquid, while Mg completely remains in the silicate. This qualitative evidence provides a plausible scenario for Si incorporation into Earth's core, potentially explaining the higher Mg/Si ratio of the bulk silicate Earth over chondritic values.

References

Albarède, F. (2009). Volatile accretion history of the terrestrial planets and dynamic implications. *Nature*, *461*(7268), 1227–1233. https://doi.org/10.1038/nature08477
Alfè, D. (2005). Melting curve of MgO from first-principles simulations. *Physical Review Letters*, *94*, 235701. https://doi.org/10.1103/PhysRevLett.94.235701
Alfè, D. (2009). Temperature of the inner-core boundary of the earth: Melting of iron at high pressure from first-principles coexistence simulations. *Physical Review B*, *79*, 060101. https://doi.org/10.1103/PhysRevB.79.060101
Alfè, D., Gillan, M. J., & Price, G. D. (2000). Constraints on the composition of the Earth's core from ab initio calculations. *Nature*, *405*(6783), 172–175. https://doi.org/10.1038/35012056
Allègre, C. J., Poirier, J. P., Humler, E., & Hofmann, A. W. (1995). The chemical composition of the earth. *Earth and Planetary Science Letters*, *134*(3-4), 515–526. https://doi.org/10.1016/0012-821X(95)00123-T
Allen, M. P., & Tildesley, D. J. (2017). *Computer Simulation of Liquids: Second Edition* (2nd ed.). Oxford: Oxford University Press. https://doi.org/10.1093/oso/9780198803195.001.0001
Antonov, V. E., Cornell, K., Fedotov, V. K., Kolesnikov, A. I., Ponyatovsky, E. G., Shiryaev, V. I., & Wipf, H. (1998). Neutron diffraction investigation of the dhcp and hcp iron hydrides and deutendes. *Journal of Alloys and Compounds*, *264*(1-2), 214–222. https://doi.org/10.1016/S0925-8388(97)00298-3
Antonov, V. E., Gurev, V. M., Kulakov, V. I., Kuzovnikov, M. A., Sholin, I. A., & Zuykova, V. Y. (2019). Solubility of deuterium and hydrogen in fcc iron at high pressures and temperatures. *Physical Review Materials*, *3*, 113604. https://doi.org/10.1103/PhysRevMaterials.3.113604
Arveson, S. M., Deng, J., Karki, B. B., & Lee, K. K. M. (2019). Evidence for Fe-Si-O liquid immiscibility at deep earth pressures. *Proceedings of the National Academy of Sciences of the United States of America*, *116*, 10,238–10,243. https://doi.org/10.1073/pnas.1821712116
Atkins, P., Julio, D. P., & Keeler, K. (2010). *Atkins' Physical Chemistry* (9th ed.). New York: W. H. Freeman and Company.

Badding, J. V., Hemley, R. J., & Mao, H. K. (1991). High-pressure chemistry of hydrogen in metals: In situ study of iron hydride. *Science*, *253*(5018), 421–424. https://doi.org/10.1126/science.253.5018.421

Badro, J., Siebert, J., & Nimmo, F. (2016). An early geodynamo driven by exsolution of mantle components from Earth's core. *Nature*, *536*(7616), 326–328. https://doi.org/10.1038/nature18594

Bajgain, S., Ghosh, D. B., & Karki, B. B. (2015). Structure and density of basaltic melts at mantle conditions from first-principles simulations. *Nature Communications*, *6*(1), 8578. https://doi.org/10.1038/ncomms9578

Belonoshko, A. B., & Dubrovinsky, L. S. (1996). Molecular dynamics of NaCl (B1 and B2) and MgO (B1) melting: Two-phase simulation. *American Mineralogist*, *81*(3-4), 303–316. https://doi.org/10.2138/am-1996-3-404

Birch, F. (1952). Elasticity and constitution of the Earth's interior. *Journal of Geophysical Research*, *57*(2), 227–286. https://doi.org/10.1029/JZ057i002p00227

Clesi, V., Bouhifd, M. A., Bolfan-Casanova, N., Manthilake, G., Schiavi, F., Raepsaet, C., et al. (2018). Low hydrogen contents in the cores of terrestrial planets. *Science Advances*, *4*(3), e1701876. https://doi.org/10.1126/sciadv.1701876

de Koker, N., & Stixrude, L. (2009). Self-consistent thermodynamic description of silicate liquids, with application to shock melting of MgO periclase and MgSiO$_3$ perovskite. *Geophysical Journal International*, *178*(1), 162–179. https://doi.org/10.1111/j.1365-246X.2009.04142.x

Dorner, F., Sukurma, Z., Dellago, C., & Kresse, G. (2018). Melting Si: Beyond density functional theory. *Physical Review Letters*, *121*, 195701. https://doi.org/10.1103/PhysRevLett.121.195701

Duan, Y., Sun, N., Wang, S., Li, X., Guo, X., Ni, H., et al. (2018). Phase stability and thermal equation of state of δ-AlOOH: Implication for water transportation to the deep lower mantle. *Earth and Planetary Science Letters*, *494*, 92–98. https://doi.org/10.1016/J.EPSL.2018.05.003

Frenkel, D., & Smit, B. (2001). *Understanding molecular simulation: From algorithms to applications* (2nd ed. pp. 167–172). London: Academic Press. https://doi.org/10.1063/1.881812

Fukai, Y. (1984). The iron-water reaction and the evolution of the earth. *Nature*, *308*(5955), 174–175. https://doi.org/10.1038/308174a0

Fukai, Y., & Suzuki, T. (1986). Iron-water reaction under high pressure and its implication in the evolution of the earth. *Journal of Geophysical Research*, *91*(B9), 9222–9230. https://doi.org/10.1029/jb091ib09p09222

Georg, R. B., Halliday, A. N., Schauble, E. A., & Reynolds, B. C. (2007). Silicon in the Earth's core. *Nature*, *447*(7148), 1102–1106. https://doi.org/10.1038/nature05927

Hirao, N., Kondo, T., Ohtani, E., Takemura, K., & Kikegawa, T. (2004). Compression of iron hydride to 80 GPa and hydrogen in the Earth's inner core. *Geophysical Research Letters*, *31*, L06616. https://doi.org/10.1029/2003gl019380

Hirose, K., Tagawa, S., Kuwayama, Y., Sinmyo, R., Morard, G., Ohishi, Y., & Genda, H. (2019). Hydrogen limits carbon in liquid iron. *Geophysical Research Letters*, *46*, 5190–5197. https://doi.org/10.1029/2019GL082591

Hirschmann, M. M., Withers, A. C., Ardia, P., & Foley, N. T. (2012). Solubility of molecular hydrogen in silicate melts and consequences for volatile evolution of terrestrial planets. *Earth and Planetary Science Letters*, *345-348*, 38–48. https://doi.org/10.1016/j.epsl.2012.06.031

Hong, Q. J., & Van De Walle, A. (2013). Solid-liquid coexistence in small systems: A statistical method to calculate melting temperatures. *Journal of Chemical Physics*, *139*, 094114. https://doi.org/10.1063/1.4819792

Hoover, W. G. (1985). Canonical dynamics: Equilibrium phase-space distributions. *Physical Review A*, *31*(3), 1695–1697. https://doi.org/10.1103/PhysRevA.31.1695

Huang, D., Badro, J., Brodholt, J., & Li, Y. (2019). Ab initio molecular dynamics investigation of molten Fe–Si–O in Earth's core. *Geophysical Research Letters*, *46*, 6397–6405. https://doi.org/10.1029/2019GL082722

Ikuta, D., Ohtani, E., Sano-Furukawa, A., Shibazaki, Y., Terasaki, H., Yuan, L., & Hattori, T. (2019). Interstitial hydrogen atoms in face-centered cubic iron in the Earth's core. *Scientific Reports*, *9*, 7108. https://doi.org/10.1038/s41598-019-43601-z

Isaev, E. I., Skorodumova, N. V., Ahuja, R., Vekilov, Y. K., & Johansson, B. (2007). Dynamical stability of Fe-H in the Earth's mantle and core regions. *Proceedings of the National Academy of Sciences*, *104*, 9168–9171. https://doi.org/10.1073/pnas.0609701104

Kresse, G., & Furthmüller, J. (1996). Efficient iterative schemes for ab initio total-energy calculations using a plane-wave basis set. *Physical Review B*, *54*(16), 11,169–11,186. https://doi.org/10.1103/PhysRevB.54.11169

Kresse, G., & Hafner, J. (1993). *Ab initio* molecular dynamics for liquid metals. *Physical Review B*, *47*(1), 558–561. https://doi.org/10.1103/PhysRevB.47.558

Kresse, G., & Joubert, D. (1999). From ultrasoft pseudopotentials to the projector augmented-wave method. *Physical Review B*, *59*(3), 1758–1775. https://doi.org/10.1103/PhysRevB.59.1758

Li, J., & Agee, C. B. (1996). Geochemistry of mantle-core differentiation at high pressure. *Nature*, *381*(6584), 686–689. https://doi.org/10.1038/381686a0

Machida, A., Saitoh, H., Sugimoto, H., Hattori, T., Sano-Furukawa, A., Endo, N., et al. (2014). Site occupancy of interstitial deuterium atoms in face-centred cubic iron. *Nature Communications*, *5*(1), 5063. https://doi.org/10.1038/ncomms6063

Malavergne, V., Bureau, H., Raepsaet, C., Gaillard, F., Poncet, M., Surblé, S., et al. (2019). Experimental constraints on the fate of H and C during planetary core-mantle differentiation.Implications for the Earth. *Icarus*, *321*, 473–485. https://doi.org/10.1016/j.icarus.2018.11.027

McDonough, W. F., & Sun, S. s. (1995). The composition of the earth. *Chemical Geology*, *120*(3-4), 223–253. https://doi.org/10.1016/0009-2541(94)00140-4

Meier, T., Trybel, F., Khandarkhaeva, S., Steinle-Neumann, G., Chariton, S., Fedotenko, T., et al. (2019). Pressure-induced hydrogen-hydrogen interaction in metallic FeH revealed by NMR. *Physical Review X*, *9*, 031008. https://doi.org/10.1103/PhysRevX.9.031008

Mookherjee, M., Stixrude, L., & Karki, B. (2008). Hydrous silicate melt at high pressure. *Nature*, *452*(7190), 983–986. https://doi.org/10.1038/nature06918

Murakami, M., Ohishi, Y., Hirao, N., & Hirose, K. (2012). A perovskitic lower mantle inferred from high-pressure, high-temperature sound velocity data. *Nature*, *485*(7396), 90–94. https://doi.org/10.1038/nature11004

Narygina, O., Dubrovinsky, L. S., McCammon, C. A., Kurnosov, A., Kantor, I. Y., Prakapenka, V. B., & Dubrovinskaia, N. A. (2011). X-ray diffraction and Mössbauer spectroscopy study of fcc iron hydride FeH at high pressures and implications for the composition of the Earth's core. *Earth and Planetary Science Letters*, *307*(3-4), 409–414. https://doi.org/10.1016/J.EPSL.2011.05.015

Nomura, R., Hirose, K., Uesugi, K., Ohishi, Y., Tsuchiyama, A., Miyake, A., & Ueno, Y. (2014). Low core-mantle boundary temperature inferred from the solidus of pyrolite. *Science*, *343*(6170), 522–525. https://doi.org/10.1126/science.1248186

Nosé, S. (1984). A unified formulation of the constant temperature molecular dynamics methods. *The Journal of Chemical Physics*, *81*(1), 511–519. https://doi.org/10.1063/1.447334

Ohira, I., Ohtani, E., Sakai, T., Miyahara, M., Hirao, N., Ohishi, Y., & Nishijima, M. (2014). Stability of a hydrous δ-phase, AlOOH-MgSiO$_2$(OH)$_2$, and a mechanism for water transport into the base of lower mantle. *Earth and Planetary Science Letters*, *401*, 12–17. https://doi.org/10.1016/j.epsl.2014.05.059

Ohtani, E., Hirao, N., Kondo, T., Ito, M., & Kikegawa, T. (2005). Iron-water reaction at high pressure and temperature, and hydrogen transport into the core. *Physics and Chemistry of Minerals*, *32*(1), 77–82. https://doi.org/10.1007/s00269-004-0443-6

Okuchi, T. (1997). Hydrogen partitioning into molten Iron at high pressure: Implications for Earth's Core. *Science*, *278*(5344), 1781–1784. https://doi.org/10.1126/science.278.5344.1781

Okuchi, T. (1998). The melting temperature of iron hydride at high pressures and its implications for the temperature of the Earth's core. *Journal of Physics. Condensed Matter*, *10*(49), 11,595–11,598. https://doi.org/10.1088/0953-8984/10/49/052

Palme, H., & O'Neill, H. (2013). Cosmochemical estimates of mantle composition. In *Treatise on Geochemistry* (Second ed., Vol. 3, pp. 1–39). Oxford: Elsevier. https://doi.org/10.1016/B978-0-08-095975-7.00201-1

Pépin, C. M., Dewaele, A., Geneste, G., Loubeyre, P., & Mezouar, M. (2014). New iron hydrides under high pressure. *Physical Review Letters*, *113*, 265504. https://doi.org/10.1103/PhysRevLett.113.265504

Pépin, C. M., Geneste, G., Dewaele, A., Mezouar, M., & Loubeyre, P. (2017). Synthesis of FeH$_5$: A layered structure with atomic hydrogen slabs. *Science*, *357*(6349), 382–385. https://doi.org/10.1126/science.aan0961

Perdew, J. P., Burke, K., & Ernzerhof, M. (1996). Generalized gradient approximation made simple. *Physical Review Letters*, *77*(18), 3865–3868. https://doi.org/10.1103/PhysRevLett.77.3865

Poirier, J. P. (1994). Light elements in the Earth's outer core: A critical review. *Physics of the Earth and Planetary Interiors*, *85*(3-4), 319–337. https://doi.org/10.1016/0031-9201(94)90120-1

Posner, E. S., & Steinle-Neumann, G. (2019). Mass transport and structural properties of binary liquid iron alloys at high pressure. *Geochemistry, Geophysics, Geosystems*, *20*, 3556–3568. https://doi.org/10.1029/2019GC008393

Rang, M., & Kresse, G. (2019). First-principles study of the melting temperature of MgO. *Physical Review B*, *99*, 184103. https://doi.org/10.1103/PhysRevB.99.184103

Righter, K. (2003). Metal-silicate partitioning of siderophile elements and core formation in the early earth. *Annual Review of Earth and Planetary Sciences*, *31*(1), 135–174. https://doi.org/10.1146/annurev.earth.31.100901.145451

Rubie, D. C., Jacobson, S. A., Morbidelli, A., O'Brien, D. P., Young, E. D., de Vries, J., et al. (2015). Accretion and differentiation of the terrestrial planets with implications for the compositions of early-formed solar system bodies and accretion of water. *Icarus*, *248*, 89–108. https://doi.org/10.1016/j.icarus.2014.10.015

Sakamaki, K., Takahashi, E., Nakajima, Y., Nishihara, Y., Funakoshi, K., Suzuki, T., & Fukai, Y. (2009). Melting phase relation of FeH$_x$ up to 20 GPa: Implication for the temperature of the Earth's core. *Physics of the Earth and Planetary Interiors*, *174*(1-4), 192–201. https://doi.org/10.1016/j.pepi.2008.05.017

Sano, A., Ohtani, E., Kondo, T., Hirao, N., Sakai, T., Sata, N., et al. (2008). Aluminous hydrous mineral δ-AlOOH as a carrier of hydrogen into the core-mantle boundary. *Geophysical Research Letters*, *35*, L03303. https://doi.org/10.1029/2007GL031718

Schwegler, E., Sharma, M., Gygi, F., & Galli, G. (2008). Melting of ice under pressure. *Proceedings of the National Academy of Sciences*, *105*, 14,779–14,783. https://doi.org/10.1073/pnas.0808137105

Shahar, A., Ziegler, K., Young, E. D., Ricolleau, A., Schauble, E. A., & Fei, Y. (2009). Experimentally determined Si isotope fractionation between silicate and Fe metal and implications for Earth's core formation. *Earth and Planetary Science Letters*, *288*(1-2), 228–234. https://doi.org/10.1016/j.epsl.2009.09.025

Siebert, J., Badro, J., Antonangeli, D., & Ryerson, F. J. (2012). Metal-silicate partitioning of Ni and co in a deep magma ocean. *Earth and Planetary Science Letters*, *321-322*, 189–197. https://doi.org/10.1016/j.epsl.2012.01.013

Takafuji, N., Hirose, K., Mitome, M., & Bando, Y. (2005). Solubilities of O and Si in liquid iron in equilibrium with (Mg,Fe)SiO$_3$ perovskite and the light elements in the core. *Geophysical Research Letters*, *32*, L06313. https://doi.org/10.1029/2005GL022773

Taniuchi, T., & Tsuchiya, T. (2018). The melting points of MgO up to 4 TPa predicted based on *ab initio* thermodynamic integration molecular dynamics. *Journal of Physics: Condensed Matter*, *30*, 114003. https://doi.org/10.1088/1361-648X/aaac96

Umemoto, K., & Hirose, K. (2020). Chemical compositions of the outer core examined by first principles calculations. *Earth and Planetary Science Letters*, *531*, 116009. https://doi.org/10.1016/j.epsl.2019.116009

Usui, Y., & Tsuchiya, T. (2010). Ab initio two-phase molecular dynamics on the melting curve of SiO2. *Journal of Earth Science*, *21*(5), 801–810. https://doi.org/10.1007/s12583-010-0126-9

Vlček, V., De Koker, N., & Steinle-Neumann, G. (2012). Electrical and thermal conductivity of Al liquid at high pressures and temperatures from ab initio computations. *Physical Review B*, *85*, 184201. https://doi.org/10.1103/PhysRevB.85.184201

Vočadlo, L., Wood, I. G., Alfè, D., & Price, G. D. (2008). Ab initio calculations on the free energy and high P–T elasticity of face-centred-cubic iron. *Earth and Planetary Science Letters*, *268*(3-4), 444–449. https://doi.org/10.1016/J.EPSL.2008.01.043

Wagle, F., & Steinle-Neumann, G. (2019). Liquid iron equation of state to the terapascal regime from ab initio simulations. *Journal of Geophysical Research: Solid Earth*, *124*, 3350–3364. https://doi.org/10.1029/2018JB016994

Wahl, S. M., & Militzer, B. (2015). High-temperature miscibility of iron and rock during terrestrial planet formation. *Earth and Planetary Science Letters*, *410*, 25–33. https://doi.org/10.1016/J.EPSL.2014.11.014

Walter, M. J., Thomson, A. R., Wang, W., Lord, O. T., Ross, J., McMahon, S. C., et al. (2015). The stability of hydrous silicates in Earth's lower mantle: Experimental constraints from the systems MgO–SiO$_2$–H$_2$O and MgO–Al$_2$O$_3$–SiO$_2$–H$_2$O. *Chemical Geology*, *418*, 16–29. https://doi.org/10.1016/J.CHEMGEO.2015.05.001

Wang, Z., & Becker, H. (2013). Ratios of S, se and Te in the silicate earth require a volatile-rich late veneer. *Nature*, *499*(7458), 328–331. https://doi.org/10.1038/nature12285

Xiong, Z., Tsuchiya, T., & Taniuchi, T. (2018). Ab initio prediction of potassium partitioning into Earth's Core. *Journal of Geophysical Research: Solid Earth*, *123*, 6451–6458. https://doi.org/10.1029/2018JB015522

Yagi, T., & Hishinuma, T. (1995). Iron hydride formed by the reaction of iron, silicate, and water: Implications for the light element of the Earth's core. *Geophysical Research Letters*, *22*(14), 1933–1936. https://doi.org/10.1029/95GL01792

Yuan, L., Ohtani, E., Ikuta, D., Kamada, S., Tsuchiya, J., Naohisa, H., et al. (2018). Chemical reactions between Fe and H$_2$O up to megabar pressures and implications for water storage in the Earth's mantle and core. *Geophysical Research Letters*, *45*, 1330–1338. https://doi.org/10.1002/2017GL075720

Zhang, Y., & Yin, Q. Z. (2012). Carbon and other light element contents in the earth's core based on first-principles molecular dynamics. *Proceedings of the National Academy of Sciences of the United States of America*, *109*, 19,579–19,583. https://doi.org/10.1073/pnas.1203826109

References From the Supporting Information

Andrault, D., Bolfan-Casanova, N., Nigro, G. L., Bouhifd, M. A., Garbarino, G., & Mezouar, M. (2011). Solidus and liquidus profiles of chondritic mantle: Implication for melting of the earth across its history. *Earth and Planetary Science Letters*, *304*(1-2), 251–259. https://doi.org/10.1016/j.epsl.2011.02.006

Fiquet, G., Auzende, A. L., Siebert, J., Corgne, A., Bureau, H., Ozawa, H., & Garbarino, G. (2010). Melting of Peridotite to 140 Gigapascals. *Science*, *329*(5998), 1516–1518. https://doi.org/10.1126/science.1192448

Le Roux, S., & Jund, P. (2010). Ring statistics analysis of topological networks: New approach and application to amorphous GeS_2 and SiO_2 systems. *Computational Materials Science*, *49*(1), 70–83. https://doi.org/10.1016/j.commatsci.2010.04.023

Rueden, C. T., Schindelin, J., Hiner, M. C., DeZonia, B. E., Walter, A. E., Arena, E. T., & Eliceiri, K. W. (2017). ImageJ2: ImageJ for the next generation of scientific image data. *BMC Bioinformatics*, *18*(1), 529. https://doi.org/10.1186/s12859-017-1934-z

Sinmyo, R., Hirose, K., & Ohishi, Y. (2019). Melting curve of iron to 290 GPa determined in a resistance-heated diamond-anvil cell. *Earth and Planetary Science Letters*, *510*, 45–52. https://doi.org/10.1016/j.epsl.2019.01.006

Stixrude, L., & Lithgow-Bertelloni, C. (2007). Influence of phase transformations on lateral heterogeneity and dynamics in Earth's mantle. *Earth and Planetary Science Letters*, *263*(1-2), 45–55. https://doi.org/10.1016/j.epsl.2007.08.027

Stukowski, A. (2010). Visualization and analysis of atomistic simulation data with OVITO-the open visualization tool. *Modelling and Simulation in Materials Science and Engineering*, *18*, 015012. https://doi.org/10.1088/0965-0393/18/1/015012

Walter, M. J., & Trønnes, R. G. (2004). Early earth differentiation. *Earth and Planetary Science Letters*, *225*(3-4), 253–269. https://doi.org/10.1016/j.epsl.2004.07.008